Water Research 285 (2025) 124056

Contents lists available at ScienceDirect

Water Research

journal homepage: www.elsevier.com/locate/watres

Unraveling the role of funnel effect vs. gutter effect in water permeance and antifouling performance of polyamide nanofiltration membranes

Chenyue Wu [a], Li Long [a,b], Zhe Yang [a,c], Yaowen Hu [a], Lu Elfa Peng [*,a], Chuyang Y. Tang [a,*]

[a] Department of Civil Engineering, The University of Hong Kong, Pokfulam, Hong Kong SAR, China
[b] School of Civil Engineering, Wuhan University, Wuhan, China
[c] Dow Centre for Sustainable Engineering Innovation, School of Chemical Engineering, The University of Queensland, Brisbane, QLD 4072, Australia

ARTICLE INFO

Keywords:
Thin-film composite (TFC) membrane
Funnel effect
Gutter effect
Intrinsic water permeability
Membrane fouling

ABSTRACT

Conventional thin-film composite (TFC) membranes often face the inherent limitation of the funnel effect. The funnel-like transport pathway, arising from water traveling transversely in the polyamide (PA) film to reach substrate pores, greatly increases the effective transport length and impairs the available water permeance. This curved transport pathway further raises a fundamental challenge for determining PA material's intrinsic water permeability. Herein, for the first time, we present a novel method to calibrate the intrinsic water permeability by accounting for this critical phenomenon. We found that the calibrated value can be several times of the apparent permeability (calculated using PA thickness without calibration). Furthermore, prompt by the disparate literature reports on the effectiveness of interlayers for mitigating funnel effect, we systematically investigated the interplay of several crucial factors (e.g., porosity and PA thickness) on the gutter/funnel effect through both experimental and modelling works. We demonstrated that the gutter effect is far more effective in enhancing water permeance and antifouling performance for membranes suffering from more severe funnel effect. For the thin-PA membrane with a low-porosity substrate, the water permeance was enhanced by approximately 75 % with the interlayer incorporation, while the flux reduction during the fouling test was significantly mitigated (i.e., from 33 % to 13 %). This work provides critical guidance on the future development of high-permeance and anti-fouling TFC membranes.

1. Introduction

Nanofiltration (NF) polyamide (PA) membranes have found a wide range of applications like water reuse and water treatment (Mohammad et al., 2015; Zhao et al., 2021). These membranes typically possess a thin-film composite (TFC) configuration with a top PA rejection film formed on a porous substrate (Cui et al., 2017; Li et al., 2016; Lu and Elimelech, 2021). The TFC structure commonly faces an inherent limitation: water travels an additional distance in the PA film longer than film thickness to reach substrate pores (Fig. 1Ai, ii). This so-called "funnel effect" severely limits the water permeance (Long et al., 2022; Lonsdale et al., 1971; Peng et al., 2022b; Ramon et al., 2012). In addition, the funnel effect can also lead to a localized high flux on the PA region spanning over the substrate pores due to the minimal hydraulic resistance, but sharply lower flux over the non-pore regions. This uneven surface flux distribution can increase fouling propensity (Gan et al., 2023; Wu et al., 2022).

Notably, the funnel-shaped curved pathway in PA films raises a critical question: which length (the actual pathway vs. the PA thickness) should be used to determine the intrinsic water permeability ($P^H_{w,Int}$) of the PA material (Fig. S1)? Water permeability is a fundamental material property that governs membrane transport behavior (Baker et al., 2010; Park et al., 2017; Ritt et al., 2022), analogous to the role of electrical conductivity in charge transport and thermal conductivity in heat transfer. Indeed, this material parameter determines the ultimate achievable membrane performance including water permeance, making it critical for the design and development of high-performance membranes (Geise et al., 2011; Park et al., 2017; Tan et al., 2018). In existing practices, researchers commonly obtain the permeability value by the product of water permeance (A) and PA layer thickness (l) (Liu et al., 2023; Wang et al., 2022b; Xue et al., 2024). However, this calculation is based on the erroneous assumption that the actual transport length equals to the PA thickness. As a result, the calculated apparent water permeability ($P^H_{w,App} = A \times l$) could show huge discrepancies up to an

---

* Corresponding authors.
E-mail addresses: elfapeng@connect.hku.hk (L.E. Peng), tangc@hku.hk (C.Y. Tang).

https://doi.org/10.1016/j.watres.2025.124056
Received 27 February 2025; Received in revised form 16 May 2025; Accepted 19 June 2025

order of magnitude for a given PA layer (Fig. S2) (Jiang et al., 2018; Wu et al., 2022), as a result of the different transport patterns for different substrate conditions. Therefore, it is urgent to develop a reliable method for evaluating intrinsic water permeability.

The funnel effect also severely compromises the water permeance. A commonly reported mitigation strategy is to incorporate an interlayer between the PA film and the substrate, which creates a “gutter effect” for shortening water transport distance in PA (Fig. 1Aiii, iv) (Cao et al., 2022; Long et al., 2022; Shi et al., 2023; Yang et al., 2020; You et al., 2021; Zhou et al., 2023; Zhu et al., 2020b). Some studies have shown great success of this strategy for boosting water permeance by nearly an order of magnitude (Cao et al., 2022; Shi et al., 2023). However, contradictory results have also been reported that interlayer incorporation may lead to marginal enhancement (Chi et al., 2022; Dai et al., 2023; Gong et al., 2019) or even reduced water permeance (Wang et al., 2017; Zhu et al., 2020a). The root cause for such disparate observations has not yet been fully explained in literature. Presumably, the funnel effect can be influenced by some crucial factors of TFC structure (i.e., substrate porosity and PA layer thickness). For example, a TFC membrane with lower substrate porosity (Wu et al., 2022) or thinner PA layer (Fig. 1Ai, ii and Fig. S3) can suffer a more severe funnel effect. In addition, according to our previous modelling work (Wang et al., 2022a), the gutter effect by interlayer would be potentially influenced by these structural factors. Therefore, a systematic experimental investigation is warranted to further examine the interplay of these crucial parameters to better elucidate their fundamental roles in membrane transport.

In this study, for the first time, we present a transport pathway-calibrated method for determining the intrinsic water permeability ($P^{H}_{w,\ Int}$) of PA material and compared it with the apparent value ($P^{H}_{w,App}$). By combining experimental investigation and model simulation, we show that $P^{H}_{w,\ Int}$ can be several times of $P^{H}_{w,App}$. Additionally, we systematically examined the interplay between the crucial factors (i.e., substrate porosity, and PA thickness) and interlayer, elucidating their critical importance for regulating the competition of the funnel and gutter effects. We show compelling evidence that interlayer inclusion can more effectively enhance water permeance and antifouling performance for membranes subject to severe funnel effect (i.e., thin PA with low-porosity substrates). Our work provides in-depth insights for future membrane design and optimization, focusing on improving separation and antifouling performance by studying the water transport mechanism in TFC nanofiltration (NF) membranes.

2. Materials and methods

2.1. Materials and chemicals

All chemicals used in this study were of ACS reagent grades. Deionized (DI) water from a Milli-Q system (Millipore, Billerica, MA) was used to prepare solutions for membrane fabrication and tests while pure n-hexane (>95%, Sigma-Aldrich, USA) was applied to prepare the organic solution for interfacial polymerization (IP) reactions. Three commercial polyethersulfone (PES) ultrafiltration (UF) membranes with different molecular weight cutoffs (MWCOs, 5k, 20k, and 150k Da, respectively) were obtained from Microdyn Nadir (Germany) as the substrates for IP reactions. These substrates were named as UP005, UP020, and UP150, respectively, according to their MWCOs. More detailed information about these three substrates can be found in our previous work (Wu et al., 2022). Piperazine (PIP, 99%) and trimesoyl chloride (TMC, 98%) were obtained from Sigma-Aldrich (USA) as monomers for IP reactions in the aqueous and organic phase, respectively. The polydopamine (PDA) interlayer was prepared by tris (hydroxymethyl, Acros Organics, Geel, Belgium), hydrochloric acid (HCl, 37 wt.%, VWR, Dorset, UK) and dopamine hydrochloride (J&K Scientific Ltd, China). Sodium chloride (NaCl, Dieckmann, China) and sodium sulfate (Na_2SO_4, Dieckmann, China) were applied to test the salt rejection of fabricated NF membranes. Toluidine blue O (TBO, Sigma-Aldrich, USA) was used to determine the density of the carboxyl group on membrane surfaces. Polyethylene glycol (PEG, molecular weight = 200, 400 and 800 Da) and ethylene glycol (EG, molecular weight = 62.07 Da) were purchased from Dieckmann (China) to determine the effective pore size of the membranes. Bovine serum albumin (BSA, Sigma-Aldrich, USA) and humic acid (Sigma-Aldrich, USA) were used as model foulants to evaluate the antifouling performance. The ionic composition of the feed solution for fouling tests were adjusted by using NaCl and calcium chloride ($CaCl_2$, Dieckmann, China) or Na_2SO_4.

2.2. Membrane fabrication

In this study, we focused on NF PA membranes since traditional NF membranes are more prone to funnel effect (Peng et al., 2022b). In comparison, this effect is minimized in reverse osmosis (RO) membranes due to nanovoids present in their PA layers (Lin et al., 2016; Peng et al., 2020). Fig. 1B shows the schematic illustration of NF membranes formed by loading free-interface PA layers on substrates (i.e., UP005, UP020,

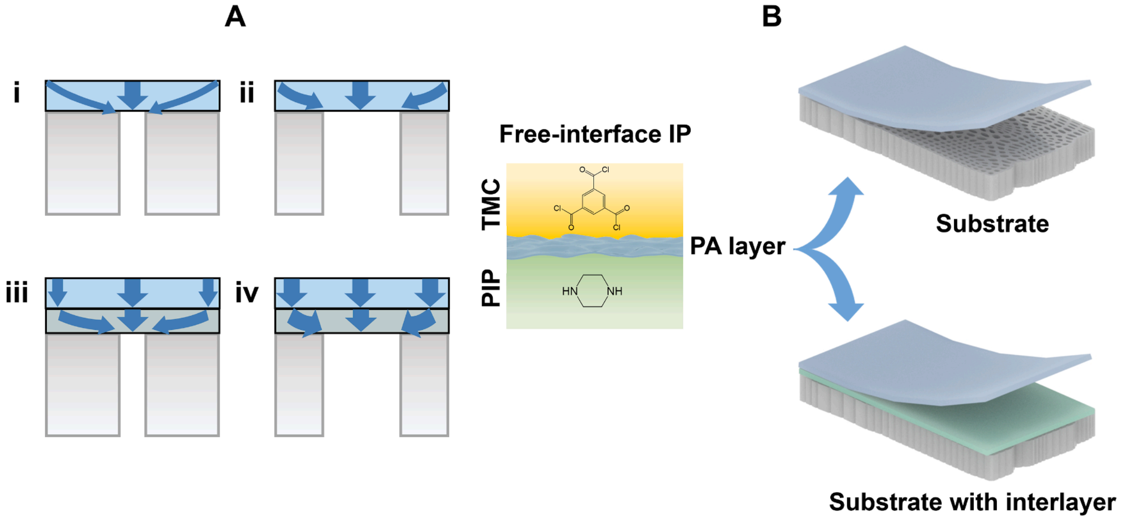

Fig. 1. (**Ai**) and (**Aii**) Various transport pathway in PA layer resulted from funnel effect. (**Aiii**) and (**Aiv**) Interlayer incorporation shorten the water transport pathways in PA layer. (**B**) Schematic illustration of NF membranes formed by loading free-interface PA layers on substrates with or without interlayer. The detailed fabrication process is presented in **Fig. S4**.

and UP150) with or without interlayer. The PA layer was fabricated at a support-free interface (Cui et al., 2017; Jiang et al., 2019; Karan et al., 2015) using 20 mL PIP solution and 10 mL TMC solution with a reaction time of 2 min. Subsequently, the formed PA layer was transferred onto a substrate (chosen from UP005, UP020, or UP150) through vacuum filtration, followed by rinsing the fabricated PA membrane with n-hexane to remove residual monomers (Fig. S4). To investigate the effect of PA thickness, different PIP solutions with the concentration of 0.02 wt.% and 0.2 wt.% were used to conduct support-free IP reactions to form thin and thick PA layers, respectively. The concentration of TMC solution was 0.1 wt.% for both thin and thick PA layers.

The PDA coating was chosen as a model interlayer to investigate the gutter effect. This coating can be easily prepared on various porous substrates and has been widely used in the literature for effectively enhancing water permeance of TFC membranes (Li et al., 2022; Shen et al., 2022). To fabricate the interlayer, a 2 g/L dopamine solution containing 10 mM Tris–HCl buffer (pH = 8.5) was poured on the surface of the substrate for 1 hour with continuous shaking (Lee et al., 2007). Then the interlayer-coated substrate was rinsed by DI water for further use.

The resultant NF membranes were labeled as Thin/Thick-s or Thin/Thick-i-s, where ‘s’ represents the MWCO of the substrate and “i” presents the interlayer incorporation (Table 1). For example, Thin-005 represents the NF membrane formed by a thin PA layer on the UP005 without a PDA interlayer while Thick-i-150 represents the NF membrane formed by a thick PA layer on the UP150 with a PDA interlayer. Previous studies have confirmed the stability of NF membranes synthesized via the free-interface approach under crossflow filtration conditions (Choi et al., 2017; Jiang et al., 2018; Wu et al., 2022).

2.3. Membrane characterization

Transmission electron microscopy (TEM, Philips CM100) was used to obtain cross-sectional micrographs to assess the thickness of a PA layer. Scanning electron microscopy (SEM, Hitachi S4800 FEG SEM) was employed for surface morphology analysis of the membranes. Fourier transform infrared spectroscopy (FTIR, Thermo Fisher Scientific) was conducted to investigate functional groups on the membrane surface. X-ray photoelectron spectroscopy (XPS, Thermo Kalpha) was applied to determine elemental compositions (e.g., O and N) of the membrane surface (Akin and Temelli, 2011; Cao et al., 2022), and the crosslinking degree of PA was calculated based on O/N ratio. An Attension Theta Goniometer (Biolin Scientific) was used to measure the water contact angle (WCA) of the membranes for the evaluation of surface hydrophilicity. TBO was applied to evaluate the surface charge by testing the carboxyl group density of membrane surfaces according to previous literatures (Mo et al., 2012; Ray et al., 2012; Tiraferri and Elimelech, 2012). Electrokinetic analyzer (Anton Paar SurPASS 3) was used to measure zeta potential of the thin and thick PA layers at pH around 7. Neutral molecular probes (i.e., PEG and EG) were used to determine the effective mean pore size and pore distribution of PA membranes (Nghiem et al., 2004; Zhang et al., 2013). A quartz crystal microbalance (QCM, E4, Q-sense Biolin Scientific) was used to determine the water absorption degree of PA layer (Lin et al., 2016). An ellipsometer (M-2000, J. A. Woollam) was used to evaluate the membrane swelling degree.

Table 1
Fabricated NF membranes with variation in substrate porosity, interlayer incorporation and PA layer thickness.

PA layer	Interlayer	Substrate		
		UP005	UP020	UP150
Thin	**without**	Thin-005	Thin-020	Thin-150
	with	Thin-i-005	Thin-i-020	Thin-i-150
Thick	**without**	Thick-005	Thick-020	Thick-150
	with	Thick-i-005	Thick-i-020	Thick-i-150

2.4. Separation performance evaluation

The assessment of separation performance, encompassing both pure water permeance and salt rejection of NF membranes, was conducted using a cross-flow filtration setup. The operation hydraulic pressure was 5 bar, and the temperature was around 25 °C. Before each test, a new membrane coupon was installed in the cross-flow test cell and pre-compacted for 1 h using DI water at 5 bar. The determination of pure water flux (J_w, L m^{-2} h^{-1}) was achieved by measuring the volume of permeate over a specified time interval, as indicated by Eq. (1):

$$J_w = \frac{\Delta V}{\Delta t \ \times S} \tag{1}$$

where V (L) is the volume of permeate, t (h) is the testing time, and S (m^2) is the effective membrane area. The pure water permeance (A, L m^{-2} h^{-1} bar^{-1}) can be calculated by the subsequent equation:

$$A = \frac{J_w}{\Delta P} \tag{2}$$

where ΔP (bar) is the applied hydraulic pressure.

To assess the salt rejection of fabricated membranes, a single salt (1000 ppm NaCl or Na_2SO_4) was used to prepare the feed solution. The determination of salt rejection (R,%) was based on the concentration difference between the feed and permeate solutions using the following Eq. (3):

$$R = \frac{C_f - C_p}{C_f} \times 100\% \tag{3}$$

where C_p and C_f are the salt concentration in the permeate and feed solution. The salt concentration was measured using the conductivity (μS/cm) that was determined by a conductivity meter (Ultrameter II, Myron L).

2.5. Transport pathway-calibrated method

The water permeation behavior of NF membranes was simulated using the commercial software COMSOL Multiphysics (v5.4) (Hu et al., 2023; Wang et al., 2022a). The simulated water permeance efficiency (η_J), defined as the ratio of the apparent membrane water permeance (A_{App-s}) over its corresponding intrinsic PA permeance (A_{Int-s}), was introduced as an important parameter for the performance evaluation (Fig. S1).

$$\eta_J = A_{App-s} / A_{Int-s} \ (0 \le \eta_J \le 1) \tag{4}$$

A_{App-s} represents the permeance of membranes that influenced by varied porosities and PA thickness (Fig. S1A), which is in turn affected by the severity of the funnel effect. This value accounts for the hydraulic resistance in both transverse and normal directions within the PA layer, and it can be obtained by performing the COMSOL simulation for the substrate supported PA layer. A_{Int-s} shows the ideal water permeance of freestanding PA layers without the substrate (i.e., substrate porosity ε = 100%, Fig. S1B). This value represents the maximum water permeance as it solely accounts for the resistance in the normal direction. η_J, which is the ratio of A_{App-s} over A_{Int-s}, represents the severity of the funnel effect. Specifically, increasing η_J from 0 to 1 indicates a reduced influence of transverse resistance on water permeance. Therefore, a greater η_J value reflects less funnel effect of the NF membrane.

By combining the experimentally obtained A_{App} and simulated η_J, the A_{Int} of the fabricated membranes are obtained as follow:

$$A_{Int} = A_{App} / \eta_J \tag{5}$$

Water permeability represents the transport property of a material.

Generally, literature obtains the observed value ($P^H_{w,\ App}$, $m^2\ s^{-1}\ Pa^{-1}$, Fig. S1C) based on A_{App} and the thickness of PA layer (Eq. (6)). However, water transport pathways influenced by funnel effect is longer than the PA thickness, this conventional calculation method potentially induce the error due to the mismatch water permeance and transport pathway length. Therefore, we calibrated the calculation of intrinsic water permeability ($P^H_{w,\ Int}$, $m^2\ s^{-1}\ Pa^{-1}$, Fig. S1D) by A_{Int} and its corresponding pathway length that equal to PA thickness (l, nm) as Eq. (7).

$$P^H_{w,\ App} = A_{App} \times l \tag{6}$$

$$P^H_{w,\ Int} = A_{Int} \times l \tag{7}$$

2.6. Antifouling testing

The evaluation of membrane antifouling performance used BSA as a model foulant. Preceding each fouling test, a new membrane coupon was pre-compacted and adjusted to the identical initial flux (J_0) of approximately 30 L m^{-2} h^{-1} (Li et al., 2007). Then, membrane fouling was tested by a feed solution containing 200 ppm BSA, 1 mM NaCl, and 0.5 mM $CaCl_2$. The first-round fouling test was sustained for 8 h, during which the water flux was measured at predetermined time intervals. The flux recorded at the 8-h corresponds to J_1. The membrane was then cleaned with DI water for 30 min under the same pressure. After DI water cleaning, the second-round fouling test was performed by a fresh foulant solution. The corresponding water flux was recorded as J_2. The irreversible flux reduction (R_{ir}) and reversible flux reduction (R_r) were evaluated using Eqs. (8) and 9 (Gan et al., 2023; Park et al., 2022):

$$R_{ir} = \frac{J_0 - J_2}{J_0} \times 100\% \tag{8}$$

$$R_r = \frac{J_2 - J_1}{J_0} \times 100\% \tag{9}$$

3. Results and discussion

3.1. Impacts of funnel effect and gutter effect on water permeance

Thin and thick PA layers (approximately 30 nm and 150 nm, respectively, Fig. 2A) were fabricated at a free interface, presenting comparable physicochemical properties (e.g., O/N, surface charge, pore size, *etc.*, Fig. S7). These PA layers were then loaded onto substrates of different porosities (3.3%, 10.8% and 21.5% for UP005, UP020 and UP150, respectively, Table S1) with or without an interlayer. As excepted, Thin-PA membranes generally present higher water permeance compared to their thicker counterparts, regardless of the presence of interlayer (Fig. 2B), which can be ascribed to the lower hydraulic resistance in thin PA layers (Jiang et al., 2020; Park et al., 2022; Sarkar et al., 2020; Wang et al., 2022b).

Interestingly, increasing porosity caused obvious enhancement in water permeance for Thin-PA membranes, yet its effect for the Thick-PA was much weaker (Fig. 2B). This can be attributed to the different transport behavior in thin vs. thick PA layers (Fig. 1A vs. Fig. S3). Conceptually, the overall hydraulic resistance in PA layers can be resolved into resistances in the normal and transverse directions (Long et al., 2022). While the resistance in the normal direction is determined by the PA thickness, that in the transverse direction is regulated by the pore-to-pore distance of the substrate (Wang et al., 2022a). For Thin-PA membranes, the overall resistance is dominantly influenced by the pore-to-pore distance (transverse resistance) compared to PA thickness (normal resistance) as Fig. 1Ai. Therefore, increasing substrate porosity, which reduces the transverse resistance, can effectively improve water permeance. While for the Thick-PA membranes governed by the normal resistance (Fig. S3Ai), varying porosity could have much less impact on the overall resistance.

Additionally, the interlayer incorporation generally yielded significant enhancement on the water permeance of Thin-PA membranes, in good agreement with previous studies (Fig. 2B) (Han et al., 2022; You et al., 2021; Zhou et al., 2023). At a fundamental level, the interlayer can effectively reduce the dominant transverse resistance in thin PA and thus increasing permeance (Fig. 1Aiii). Notably, at the highest substrate porosity of 21.5%, the interlayer only had a marginal effect in enhancing permeance due to the shorter pore-to-pore distance of the substrate. In contrast, the interlayer had no major impact on permeance for Thick-PA membranes (Fig. 2B) whose overall resistance is dominated by that in the normal direction. Interestingly, the permanence of Thick-i-150 with interlayer incorporation was even slightly lower than that of Thick-150 (Fig. 2B), suggesting that the additional normal resistance introduced by the interlayer overweighs the reduction in transverse resistance in the PA layer.

3.2. Severity of funnel effect and efficiency of gutter effect

Fig. 3A presents the experimentally obtained apparent water permeance (A_{App}). Even with an identical rejection layer (e.g., for the Thin-

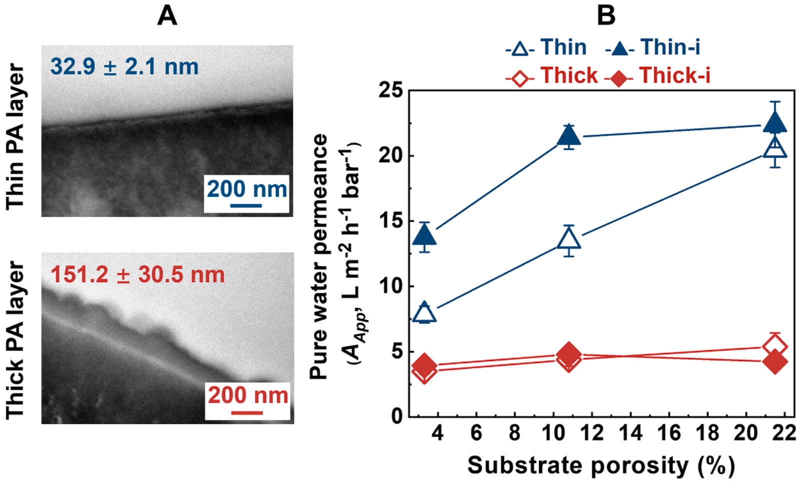

Fig. 2. (**A**) TEM characterized thickness of thin and thick PA layers. The thickness was obtained by taking the average of ten thickness values based on TEM images (**Fig. S6**) using Image-Pro Plus (Media Cybernetics, Inc.).(Peng et al., 2020) (**B**) Pure water permeance of NF membranes. Testing conditions: the cross-flow filtration experiments were conducted under a hydraulic pressure of 5 bar at a temperature of 25 °C. Rejection performance of the membranes is presented in **Fig. S8**. The data for Thin-PA membranes (hollow triangles) were obtained from our previous study (Wu et al., 2022), and all other data were measured in the current study.

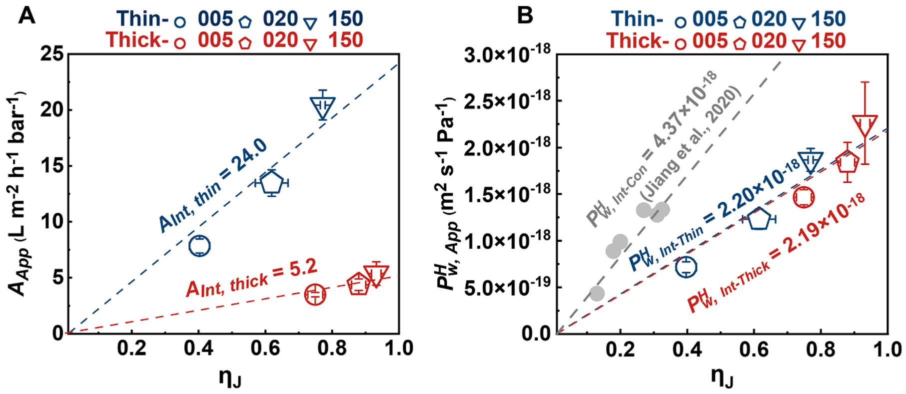

Fig. 3. (**A**) Experimental and simulated results of water permeance for thin- and thick-PA membranes, and (**B**)water permeability of PA fabricated by free-interface IP (current study) and conventional IP (Jiang et al., 2020). The nearly identical $P^H_{w,\ Int}$ values may be attributed to the comparable physicochemical properties of PA layers (**Fig. S7**). A_{App} is the experimental water permeance and the water permeance efficiency ($\eta_J = A_{App-s}/A_{Int-s}$) was calculated based on the 3D model. A_{Int} of fabricated PA layer was calculated by $A_{Int} = A_{App}/\eta_J$ as the slope. Water permeability was calculated by apparent or intrinsic water permeance, respectively. The water permeability of PA fabricated by conventional IP is calculated using the data collected from the literature (Hu et al., 2025; Jiang et al., 2020).

PA membranes), these membranes had dramatically different A_{App} values, which is attributed to their different degrees of funnel effect. This observation implies that the traditional way of calculating membrane permeability (Freeman, 1999; Liu et al., 2023; Robeson et al., 2015; Tan et al., 2018) by the product of experimentally obtained apparent permeance and the thickness of the rejection layer may not be reliable and have to be corrected for the funnel effect. To evaluate the impacts of funnel effect, a 3D model (Wang et al., 2022a) considering substrate porosity and PA thickness was applied to determine the water permeance efficiency (η_J, ranging from 0 to 1) – a parameter defined as the ratio of apparent water permeance (A_{App}) to intrinsic water permeance (A_{Int}). In general, membranes with smaller porosity or thinner PA layer tend to have lower η_J values as a result of their more severe funnel effect (Fig. 1Ai, ii and Fig. S3).

Notably, a strong linear correlation between the experimentally obtained A_{App} and simulated η_J was observed (Fig. 3A). It allows us to evaluate the intrinsic water permeance (A_{Int}) of the fabricated membranes, as indicated by the slope of the fitting lines. The A_{Int} value for the Thin-PA membranes (24.0 L m^{-2} h^{-1} bar^{-1}) was approximatively 5 times of that for the Thick-PA membranes (5.2 L m^{-2} h^{-1} bar^{-1}), which can be rationalized by their difference in PA layer thickness (32.9 nm vs. 151.2 nm, see in TEM, Fig. S6). Indeed, one could normalize the intrinsic water permeance by the corresponding PA layer thickness, with the product $A_{Int} \times l$ signifies the intrinsic water permeability ($P^H_{w,\ Int}$) – a fundamental material property (Liang et al., 2018). In general, one would expect different fitting lines for water permeability due to the different material properties. Coincidentally, Fig. 3B shows nearly identical $P^H_{w,\ Int}$ values for the two sets of membranes (~2.2 × 10^{-18} m^2 s^{-1} Pa^{-1} or 7.9 × 10^{-7} L m^{-1} h^{-1} bar^{-1}), which may be explained by the membrane characterization results (Fig. S7). For example, the cross-linking degree (Fig. S7G) and carboxyl group density (Fig. S7H) were similar for the thin- and thick-PA layers. Although the two PA layers show slightly different surface hydrophilicity (Fig. S7E) and pore radius (Fig. S7J), the effect of a more hydrophilic surface of the thick-PA layer (that promotes water permeance) offsets that of its smaller pore size (which reduces permeance).

We further adopted the experimental data of a series of conventional membranes with known thickness from a previous study (Jiang et al., 2020), which allows plotting apparent permeability against the water permeation efficiency (Hu et al., 2025). The linear fitting ($P^H_{w,Int-Con}$) indicates that the calibration method of intrinsic permeability is readily expanded for conventional membranes. Based on this fitting, the conventional membranes prepared by Jiang et al. (2020) had an intrinsic permeability of 4.37 × 10^{-18} m^2 s^{-1} Pa^{-1}, which was greater (but still on the same order of magnitude) compared to that for the thin- and thick-PA layers reported in the current study. According to the literature, conventionally prepared PA films typically have a looser structure compared to those prepared at a free interface due to the limited PIP supply in the former case (Peng et al., 2022a; Trivedi et al., 2018), which explains the higher intrinsic permeability observed for the conventional PA films.

Fig. 4A,B provide a convenient framework to better quantify the influence of water transport path on water permeance, where A_{App} is plotted as a function of the substrate porosity for both Thin- and Thick-PA membranes. In the same figure, we also include (a) the ideal water permeance (A_{Int}), which is the upper bound value (Park et al., 2017; Robeson, 1991; 2008) represents the maximum water permeance obtainable at substrate porosity of 100 % (i.e., assuming the entire PA area contributes to the permeance); and (b) the substrate-limited lower bound value (εA_{Int}) (Wang et al., 2022a), which assumes that only the pore-spanning region (dark blue area, Fig. 4C) contributes to water transport. For typical TFC membranes, their A_{App} values lie between the two bounds (Fig. 4A,B), since the PA region adjacent to the substrate pore (the funnel region indicated by the light blue area, Fig. 4C) would also partially contribute to the permeance. Nevertheless, the region far away from the pore (the blind region indicated by the gray area, Fig. 4C) could not transport water effectively, causing the apparent water permeance to be much lower than the ideal value A_{Int}, particularly for Thin-PA membranes with low substrate porosity (Fig. 4A). In comparison, Thick-PA membranes exhibit lower ideal water permeance (Fig. 4B) and weakened funnel effect (Fig. 4 Ci vs. Di).

Interlayer incorporation could efficiently reduce the blind region, thereby enhancing the water permeance. For a Thin-PA membrane with a low substrate porosity that suffers from the severest funnel effect, the presence of interlayer greatly extends the available region for water collection (light blue region, Fig. 4 Ci vs. Cii). Nevertheless, this effect diminishes for membranes with less severe funnel effect, e.g., increased substrate porosity (Fig. 4A) or PA thickness (Fig. 4B; Fig. 4 Di vs. Dii). For cases involving excessively long pore-to-pore distance, the transverse resistance through the interlayer could still be substantial to cause some minor blind regions. In general, to avoid such problems, $P^H_{w,\ Int-IL} \times l_{IL} < P^H_{w,\ Int-PA} \times l_{PA}$ need to be achieved (Wang et al., 2022a).

3.3. Effects of transport pathway on membrane fouling propensity

According to the literature, hydrodynamic conditions (e.g., water flux, cross flow) play a crucial role in membrane fouling (Li et al., 2007; Liu et al., 2018; Wu et al., 2022). For example, a more severe fouling can

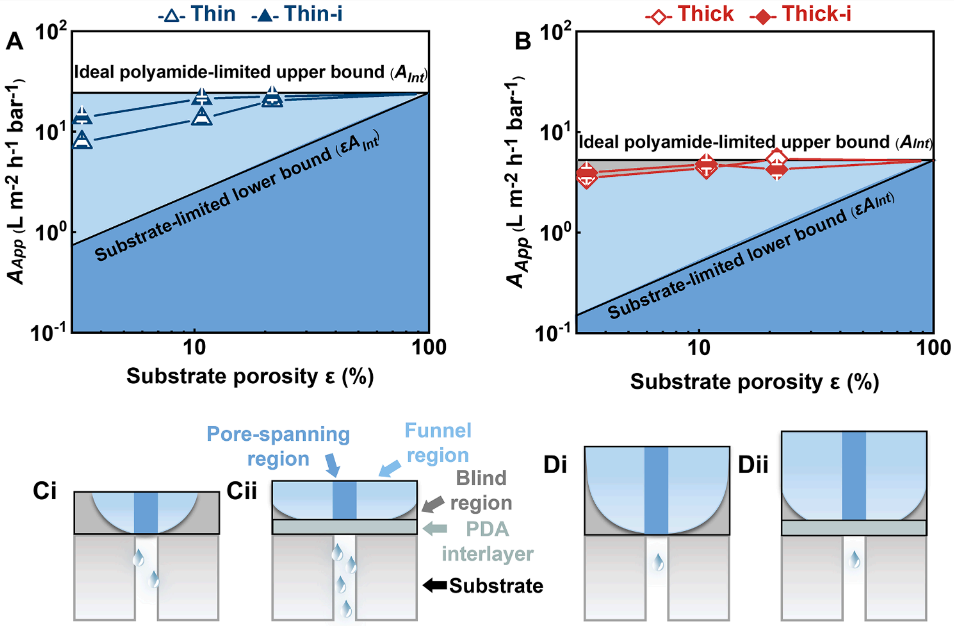

Fig. 4. Substrate porosity was a function of A_{App} and A_{Int} for (**A**) thin- and (**B**) thick-PA membrane, respectively. In PA layers, water permeance comes from different regions in (**Ci**) (**Cii**) thin and (**Di**) (**Dii**) thick PA-layer membranes with/without interlayer, including pore-spanning region (dark blue area), funnel region (light blue area) and blind region (gray area). Notably, the interlayer can minimize the blind region by reducing transverse resistance in the PA layer.

occur at higher water flux (Bacchin et al., 2006; Li et al., 2007). Recent studies have demonstrated that the funnel effect can lead to non-uniform flux distribution (Fig. 1A) and localized high-flux hot spots on pore-spanning PA regions (Fig. S10) (Gan et al., 2023; Long et al., 2022). As a result, a more severe funnel effect tends to increase fouling propensity. In contrast, the gutter effect can reduce fouling tendency by mitigating the funnel effect. Fig. 5A, B presents the fouling propensities for the above series of membranes. For the membranes with a low-porosity substrate (Fig. 5A), Thin-005 presents more obvious flux reduction than that of Thick-005, which can be explained by the more severe funnel effect of the thin-PA membrane (Wu et al., 2022). Specifically, funnel effect can cause uneven flux distribution with localized "hot spots" of high-flux above pore-spanning regions (indicated by thicker arrow, Fig. 1Ai) (Gan et al., 2023; Ramon et al., 2012; Tang et al., 2007). Such high-flux hot spots can accelerate the accumulation of foulants (Fig. S10) (Tang et al., 2011), resulting in more severe membrane fouling. In addition, both Thin- and Thick-PA membranes with interlayer incorporation experienced less flux reduction (Fig. 5A,C) compared to their counterparts without an interlayer. This mitigated fouling propensity can be attributed to the interlayer-induced gutter effect, which could improve the uniformity of flux distribution with less hot spots over the PA surface (Fig. 1Aiii) (Long et al., 2022; Wang et al., 2022a). In contrast to the low-porosity substrate counterparts, the benefits of thicker film and interlayer incorporation were less obvious for the high-porosity counterpart (Fig. 5B) due to the less severe funnel effect offered by larger substrate porosity (Wu et al., 2022).

Fig. 5C shows the relationship between total flux reduction and η_J. For example, the interlayer-incorporated membranes, generally featuring η_J values close to unity, tend to have lower flux reduction (solid symbols in Fig. 5C). In comparison, membranes with low η_J values (e.g., $\eta_J = 0.36$ for Thin-005) exhibited much severer flux reduction. As discussed earlier, η_J is a direct indicator for the severity of funnel effect, which in turn affects the uniformity of the flux distribution over the membrane surface (indicated by arrows in Fig. 1Ai). For fouling tests conducted under an identical flux of 30 L m^{-2} h^{-1} (representing the average flux over the membrane surface), a lower η_J value translates into a higher localized maximum flux (Wang et al., 2022a), which promotes faster fouling (Gan et al., 2023; Long et al., 2022; Wu et al., 2022).

In the current study, the fouled membranes were cleaned with DI water to evaluate fouling reversibility. As shown in Fig. 6A,B, membranes with an interlayer or increased substrate porosity/PA thickness gave less irreversible fouling (e.g., Thin-005 vs. Thick-005), which is well corresponded to their higher η_J values (Fig. S7A). These observations once again confirmed the better antifouling performance of polyamide membranes with enhanced gutter effect or mitigated funnel effect. Additionally, the reversible flux reduction of all NF membranes shows marginal difference (Fig. 7B), which can be potentially attributed to the identical cleaning process. These observations once again confirmed the better antifouling performance of polyamide membranes with enhanced gutter effect or mitigated funnel effect.

3.4. Perspective

As a fundamental material property governing membrane transport behavior, intrinsic water permeability ($P^H_{w,Int}$) can reveal the role of material properties on membrane performance and corroborate molecular dynamics simulation results. However, the traditional calculation method ($P^H_{w,App}$), which directly uses film thickness without accounting for the actual transport pathway, may lead to discrepancies of up to an order of magnitude compared to the actual (intrinsic) values (Fig. S2). To better reflect the actual material properties, future studies should adopt the pathway-calibrated $P^H_{w,Int}$ for membrane design and modeling. In essence, this novel calibration approach normalizes the experimental/apparent water permeance by the actual PA thickness together with the theoretical water permeance efficiency. To overcome the tedious procedures involved, future studies may establish a comprehensive database on the chemistry-property relationship of membrane materials (analogous to the Open Membrane Database (Ritt et al., 2022)), which documents reference permeability values for given membrane recipes.

4. Conclusions

This study unravels the roles of funnel effect and gutter effect in the separation and antifouling performance of TFC NF membranes. In gen-

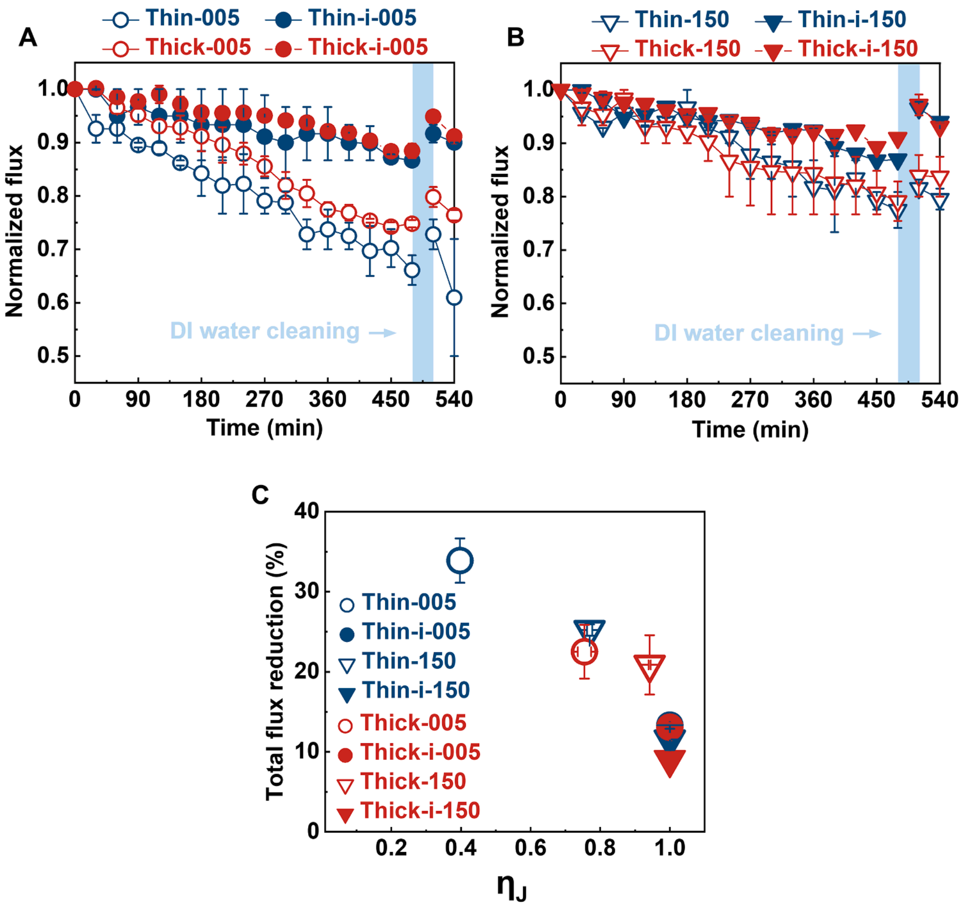

Fig. 5. Fouling test results of membranes with/without interlayer incorporation and with varied PA film thickness on the substrates of (**A**) UP005 and (**B**) UP150. Test conditions: the feed solution contains 200 ppm BSA, 0.1 mM NaCl and 0.5 mM $CaCl_2$. An identical initial water flux of approximately 30 L m^{-2} h^{-1} was used by adjusting the hydraulic pressure. All tests were conducted in duplicates for each membrane and the error bars represented the range based on the two replicates. The data for Thin-005 and Thin-150 were obtained from our pervious study,(Wu et al., 2022) and all other data were measured in the current study. (**C**) The relationship between water permeance efficiency (η_J) and total flux reduction.

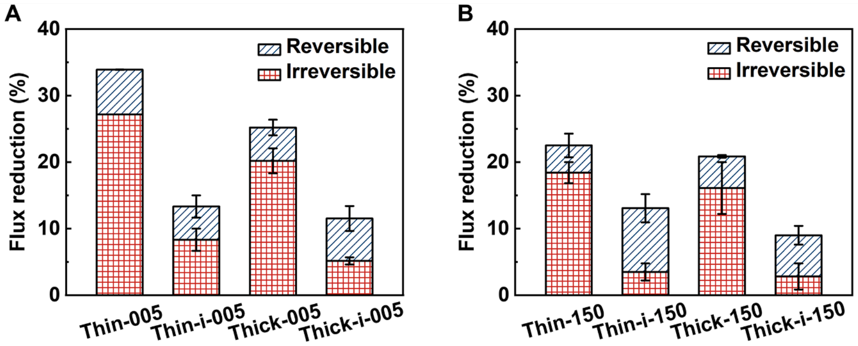

Fig. 6. Reversible and irreversible flux reduction in fouling tests of membranes with (**A**) UP005 and (**B**) UP150 substrate. All tests were conducted in duplicates for each membrane and the error bars represented the range based on the two replicates.

eral, membranes with mitigated funnel effect and/or enhanced gutter effect exhibited better antifouling performance thanks to their improved uniformity of flux distribution (see in Supporting Information S9). In addition, for the first time, we present a transport pathway-calibrated method to determine the intrinsic water permeability ($P^{H}_{w,Int}$). This intrinsic value was found to be several times higher than the apparent value in the current study, suggesting a huge risk of greatly underestimating the true permeability of membrane materials using the conventional method. Overall, the mechanistic insights on water transport/fouling behaviors and the transport pathway-calibrated method gained in the current work can pave a fundamental stone for the future development of NF polyamide membranes.

CRediT authorship contribution statement

Chenyue Wu: Conceptualization, Investigation, Methodology, Visualization, Writing – original draft. **Li Long:** Conceptualization, Methodology, Validation, Writing – original draft. **Zhe Yang:**

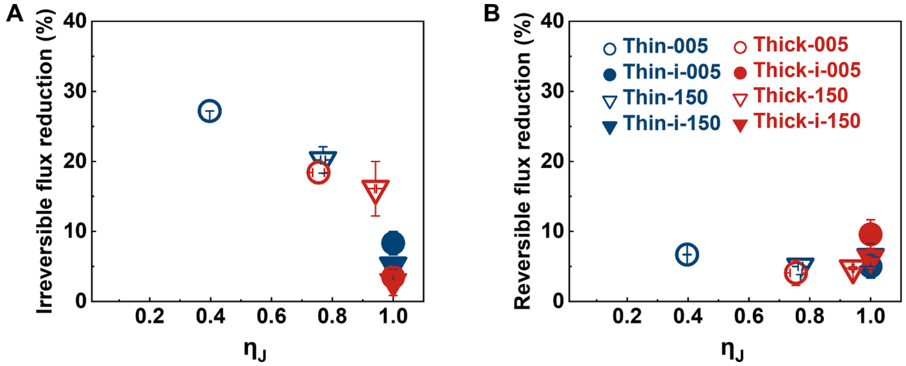

Fig. 7. The relationship between water permeance efficiency (η_J) and (**A**) irreversible flux reduction, (**B**) reversible flux reduction.

Conceptualization, Formal analysis, Methodology, Software. **Yaowen Hu:** Investigation, Methodology. **Lu Elfa Peng:** Investigation, Visualization, Writing – review & editing. **Chuyang Y. Tang:** Conceptualization, Supervision, Writing – review & editing.

Declaration of competing interest

The authors declare that they have no known competing financial interests or personal relationships that could have appeared to influence the work reported in this paper.

Acknowledgment

This work was substantially supported by the General Research Fund (Project #17201921) of the Research Grants Council of Hong Kong. The work was also partially sponsored by Seed Funding for Strategic Interdisciplinary Research Scheme (Project #102010174), Seed Funding for Basic Research (Project #202111159075), and Outstanding Researcher Award (Project #102010224) from The University of Hong Kong. We also appreciate the Electron Microscopic Unit (EMU) at The University of Hong Kong for the assistance of SEM and TEM characterization. The QCM measurement was supported by the URC Small Equipment Fund (Project #102010138) of The University of Hong Kong.

Supplementary materials

Supplementary material associated with this article can be found, in the online version, at doi:10.1016/j.watres.2025.124056.

Data availability

Data will be made available on request.

References

Akin, O., Temelli, F., 2011. Probing the hydrophobicity of commercial reverse osmosis membranes produced by interfacial polymerization using contact angle, XPS, FTIR, FE-SEM and AFM. Desalination 278 (1–3), 387–396.

Bacchin, P., Aimar, P., Field, R., 2006. Critical and sustainable fluxes: theory, experiments and applications. J. Membr. Sci. 281 (1–2), 42–69.

Baker, R.W., Wijmans, J.G., Huang, Y., 2010. Permeability, permeance and selectivity: a preferred way of reporting pervaporation performance data. J. Membr. Sci. 348 (1–2), 346–352.

Cao, S., Deshmukh, A., Wang, L., Han, Q., Shu, Y., Ng, H.Y., Wang, Z., Lienhard, J.H., 2022. Enhancing the permselectivity of thin-film composite membranes interlayered with MoS(2) nanosheets via precise thickness control. Environ. Sci. Technol. 56 (12), 8807–8818.

Chi, M., Zheng, P., Wei, M., Zhu, A., Zhong, L., Zhang, Q., Liu, Q., 2022. Polyamide composite nanofiltration membrane modified by nanoporous TiO2 interlayer for enhanced water permeability. J. Ind. Eng. Chem. 115, 230–240.

Choi, W., Jeon, S., Kwon, S.J., Park, H., Park, Y.-I., Nam, S.-E., Lee, P.S., Lee, J.S., Choi, J., Hong, S., Chan, E.P., Lee, J.-H., 2017. Thin film composite reverse osmosis membranes prepared via layered interfacial polymerization. J. Membr. Sci. 527, 121–128.

Cui, Y., Liu, X.-Y., Chung, T.-S., 2017. Ultrathin polyamide membranes fabricated from free-standing interfacial polymerization: synthesis, modifications, and post-treatment. Ind. Eng. Chem. Res. 56 (2), 513–523.

Dai, R., Chen, J., Han, H., Zhou, H., Wang, Z., 2023. Interfacial wettability regulation enables one-step upcycling of the end-of-life polymeric microfiltration membrane. ACS ES&T Eng. 3 (4), 479–486.

Freeman, B.D., 1999. Basis of permeability/selectivity tradeoff relations in polymeric gas separation membranes. Macromolecules 32 (2), 375–380.

Gan, Q., Wu, C., Long, L., Peng, L.E., Yang, Z., Guo, H., Tang, C.Y., 2023. Does surface roughness necessarily increase the fouling propensity of polyamide reverse osmosis membranes by humic acid? Environ. Sci. Technol. 57 (6), 2548–2556.

Geise, G.M., Park, H.B., Sagle, A.C., Freeman, B.D., McGrath, J.E., 2011. Water permeability and water/salt selectivity tradeoff in polymers for desalination. J. Membr. Sci. 369 (1–2), 130–138.

Gong, G., Wang, P., Zhou, Z., Hu, Y., 2019. New insights into the role of an interlayer for the fabrication of highly selective and permeable thin-film composite nanofiltration membrane. ACS Appl. Mater. Interfaces 11 (7), 7349–7356.

Han, S., Zhu, J., Uliana, A.A., Li, D., Zhang, Y., Zhang, L., Wang, Y., He, T., Elimelech, M., 2022. Microporous organic nanotube assisted design of high performance nanofiltration membranes. Nat. Commun. 13 (1), 7954.

Hu, Y., Sarkar, P., Peng, L.E., Wang, F., Yang, Z., Tang, C.Y., 2025. Design ultrathin polyamide membranes against funnel effect: a novel zone-of-influence-based approach. Environ. Sci. Technol. https://doi.org/10.1021/acs.est.5c01365.

Hu, Y., Wang, F., Yang, Z., Tang, C.Y., 2023. Modeling nanovoid-enhanced water permeance of thin film composite membranes. J. Membr. Sci. 675, 121555.

Jiang, C., Zhang, L., Li, P., Sun, H., Hou, Y., Niu, Q.J., 2020. Ultrathin film composite membranes fabricated by novel In situ free interfacial polymerization for desalination. ACS Appl. Mater. Interfaces 12 (22), 25304–25315.

Jiang, Z., Karan, S., Livingston, A.G., 2018. Water transport through ultrathin polyamide nanofilms used for reverse osmosis. Adv. Mater. 30 (15), 1705973.

Jiang, Z., Karan, S., Livingston, A.G., 2019. Membrane Fouling: does microscale roughness matter? Ind. Eng. Chem. Res. 59 (12), 5424–5431.

Karan, S., Jiang, Z., Livingston, A.G., 2015. Sub–10 nm polyamide nanofilms with ultrafast solvent transport for molecular separation. Science 348 (6241), 1347–1351.

Lee, H., Dellatore, S.M., Miller, W.M., Messersmith, P.B., 2007. Mussel-inspired surface chemistry for multifunctional coatings. Science 318 (5849), 426–430.

Li, B., Ke, X.-X., Yuan, Z.-H., Zhong, L.-B., Zhao, Q.-B., Zheng, Y.-M., 2022. High performance electrospun thin-film composite forward osmosis membrane by tailoring polyamide active layer with polydopamine interlayer for desulfulrization wastewater desalination. Desalination 534, 115781.

Li, D., Yan, Y., Wang, H., 2016. Recent advances in polymer and polymer composite membranes for reverse and forward osmosis processes. Prog. Polym. Sci. 61, 104–155.

Li, Q., Xu, Z., Pinnau, I., 2007. Fouling of reverse osmosis membranes by biopolymers in wastewater secondary effluent: role of membrane surface properties and initial permeate flux. J. Membr. Sci. 290 (1–2), 173–181.

Liang, B., Li, Q., Cao, B., Li, P., 2018. Water permeance, permeability and desalination properties of the sulfonic acid functionalized composite pervaporation membranes. Desalination 433, 132–140.

Lin, L., Lopez, R., Ramon, G.Z., Coronell, O., 2016. Investigating the void structure of the polyamide active layers of thin-film composite membranes. J. Membr. Sci. 497, 365–376.

Liu, J., Wang, Z., Tang, C.Y., Leckie, J.O., 2018. Modeling dynamics of colloidal fouling of RO/NF membranes with A novel collision-attachment approach. Environ. Sci. Technol. 52 (3), 1471–1478.

Liu, Y., Wang, K., Cheng, P., Fan, K., Gao, Y., Xia, S., Wang, X.-m., Xie, Y.F., Huang, X., 2023. Hexane treatment to facilely tailor polyamide nanofiltration membrane performance: the critical role of treatment duration. ACS ES&T Eng. 3 (11), 1706–1715.

Long, L., Wu, C., Yang, Z., Tang, C.Y., 2022. Carbon nanotube interlayer enhances water permeance and antifouling performance of nanofiltration membranes: mechanisms and experimental evidence. Environ. Sci. Technol. 56 (4), 2656–2664.

Lonsdale, H.K., Riley, R.L., Lyons, C.R., Carosella, D.P., 1971. Membrane Processes in Industry and Biomedicine. Springer, pp. 101–122.

Lu, X., Elimelech, M., 2021. Fabrication of desalination membranes by interfacial polymerization: history, current efforts, and future directions. Chem. Soc. Rev. 50 (11), 6290–6307.

Mo, Y., Tiraferri, A., Yip, N.Y., Adout, A., Huang, X., Elimelech, M., 2012. Improved antifouling properties of polyamide nanofiltration membranes by reducing the density of surface carboxyl groups. Environ. Sci. Technol. 46 (24), 13253–13261.

Mohammad, A.W., Teow, Y.H., Ang, W.L., Chung, Y.T., Oatley-Radcliffe, D.L., Hilal, N., 2015. Nanofiltration membranes review: recent advances and future prospects. Desalination 356, 226–254.

Nghiem, L.D., Schäfer, A.I., Elimelech, M., 2004. Removal of natural hormones by nanofiltration membranes: measurement, modeling, and mechanisms. Environ. Sci. Technol. 38 (6), 1888–1896.

Park, H.B., Kamcev, J., Robeson, L.M., Elimelech, M., Freeman, B.D., 2017. Maximizing the right stuff: the trade-off between membrane permeability and selectivity. Science 356 (6343), eaab0530.

Park, S.-J., Lee, M.-S., Choi, W., Lee, J.-H., 2022. Biocidal surfactant-assisted fabrication of thin film composite membranes with excellent and durable anti-biofouling performance. Chem. Eng. J. 431, 134114.

Peng, L.E., Gan, Q., Yang, Z., Wang, L., Sun, P.-F., Guo, H., Park, H.-D., Tang, C.Y., 2022a. Deciphering the role of amine concentration on polyamide formation toward enhanced RO performance. ACS ES&T Eng. 2 (5), 903–912.

Peng, L.E., Yang, Z., Long, L., Zhou, S., Guo, H., Tang, C.Y., 2022b. A critical review on porous substrates of TFC polyamide membranes: mechanisms, membrane performances, and future perspectives. J. Membr. Sci. 641, 119871.

Peng, L.E., Yao, Z., Yang, Z., Guo, H., Tang, C.Y., 2020. Dissecting the role of substrate on the morphology and separation properties of thin film composite polyamide membranes: seeing is believing. Environ. Sci. Technol. 54 (11), 6978–6986.

Ramon, G.Z., Wong, M.C.Y., Hoek, E.M.V., 2012. Transport through composite membrane, part 1: is there an optimal support membrane? J. Membr. Sci. 415-416, 298–305.

Ray, J.R., Lee, B., Baltrusaitis, J., Jun, Y.S., 2012. Formation of iron(III) (hydr)oxides on polyaspartate- and alginate-coated substrates: effects of coating hydrophilicity and functional group. Environ. Sci. Technol. 46 (24), 13167–13175.

Ritt, C.L., Stassin, T., Davenport, D.M., DuChanois, R.M., Nulens, I., Yang, Z., Ben-Zvi, A., Segev-Mark, N., Elimelech, M., Tang, C.Y., Ramon, G.Z., Vankelecom, I.F.J., Verbeke, R., 2022. The open membrane database: synthesis–structure–performance relationships of reverse osmosis membranes. J. Membr. Sci. 641, 119927.

Robeson, L.M., 1991. Correlation of separation factor versus permeability for polymeric membranes. J. Membr. Sci. 62 (2), 165–185.

Robeson, L.M., 2008. The upper bound revisited. J. Membr. Sci. 320 (1–2), 390–400.

Robeson, L.M., Liu, Q., Freeman, B.D., Paul, D.R., 2015. Comparison of transport properties of rubbery and glassy polymers and the relevance to the upper bound relationship. J. Membr. Sci. 476, 421–431.

Sarkar, P., Modak, S., Karan, S., 2020. Ultraselective and highly permeable polyamide nanofilms for ionic and molecular nanofiltration. Adv. Funct. Mater. 31 (3), 2007054.

Shen, Q., Lin, Y., Ueda, T., Zhang, P., Jia, Y., Istirokhatun, T., Song, Q., Guan, K., Yoshioka, T., Matsuyama, H., 2022. The underlying mechanism insights into support polydopamine decoration toward ultrathin polyamide membranes for high-performance reverse osmosis. J. Membr. Sci. 646, 120269.

Shi, Y., Wang, Z., Mai, Z., Shen, Q., Song, Q., Fu, W., Xiang, S., Fang, S., Zhang, P., Chiao, Y.-H., Guan, K., Matsuyama, H., 2023. Nanomorphogenesis of template-induced crumpled polyamide nanofiltration membranes. J. Membr. Sci. 686, 121997.

Tan, Z., Chen, S., Peng, X., Zhang, L., Gao, C., 2018. Polyamide membranes with nanoscale turing structures for water purification. Science 360 (6388), 518–521.

Tang, C.Y., Chong, T.H., Fane, A.G., 2011. Colloidal interactions and fouling of NF and RO membranes: a review. Adv. Colloid Interface Sci. 164 (1–2), 126–143.

Tang, C.Y., Fu, Q.S., Criddle, C.S., Leckie, J.O., 2007. Effect of flux (Transmembrane Pressure) and membrane properties on fouling and rejection of reverse osmosis and nanofiltration membranes treating perfluorooctane sulfonate containing wastewater. Environ. Sci. Technol. 41 (6), 2008–2014.

Tiraferri, A., Elimelech, M., 2012. Direct quantification of negatively charged functional groups on membrane surfaces. J. Membr. Sci. 389, 499–508.

Trivedi, J.S., Bhalani, D.V., Bhadu, G.R., Jewrajka, S.K., 2018. Multifunctional amines enable the formation of polyamide nanofilm composite ultrafiltration and nanofiltration membranes with modulated charge and performance. J. Mater. Chem. A 6 (41), 20242–20253.

Wang, F., Yang, Z., Tang, C.Y., 2022a. Modeling water transport in interlayered thin-film nanocomposite membranes: gutter effect vs funnel effect. ACS ES&T Engg 2 (11), 2023–2033.

Wang, J.-J., Yang, H.-C., Wu, M.-B., Zhang, X., Xu, Z.-K., 2017. Nanofiltration membranes with cellulose nanocrystals as an interlayer for unprecedented performance. J. Mater. Chem. A 5 (31), 16289–16295.

Wang, K., Fu, W., Wang, X.M., Xu, C., Gao, Y., Liu, Y., Zhang, X., Huang, X., 2022b. Molecular design of the polyamide layer structure of nanofiltration membranes by sacrificing hydrolyzable groups toward enhanced separation performance. Environ. Sci. Technol. 56 (24), 17955–17964.

Wu, C., Long, L., Yang, Z., Tang, C.Y., 2022. Porous substrate affects fouling propensity of thin-film composite nanofiltration membranes. J. Membr. Sci. Lett. 2 (2), 100036.

Xue, Y.R., Liu, C., Ma, Z.Y., Zhu, C.Y., Wu, J., Liang, H.Q., Yang, H.C., Zhang, C., Xu, Z.K., 2024. Harmonic amide bond density as a game-changer for deciphering the crosslinking puzzle of polyamide. Nat Commun 15 (1), 1539.

Yang, Z., Sun, P.F., Li, X., Gan, B., Wang, L., Song, X., Park, H.D., Tang, C.Y., 2020. A critical review on thin-film nanocomposite membranes with interlayered structure: mechanisms, recent developments, and environmental applications. Environ. Sci. Technol. 54 (24), 15563–15583.

You, X., Xiao, K., Wu, H., Li, Y., Li, R., Yuan, J., Zhang, R., Zhang, Z., Liang, X., Shen, J., Jiang, Z., 2021. Electrostatic-modulated interfacial polymerization toward ultra-permselective nanofiltration membranes. iScience 24 (4), 102369.

Zhang, S., Fu, F., Chung, T.-S., 2013. Substrate modifications and alcohol treatment on thin film composite membranes for osmotic power. Chem. Eng. Sci. 87, 40–50.

Zhao, Y., Tong, T., Wang, X., Lin, S., Reid, E.M., Chen, Y., 2021. Differentiating solutes with precise nanofiltration for next generation environmental separations: a review. Environ. Sci. Technol. 55 (3), 1359–1376.

Zhou, H., Qiu, Z., Zeng, J., Dai, R., Wang, Z., 2023. Ultra-permeable polyamide nanofiltration membrane modified by hydrophilic-hydrophobic alternated lignocellulosic nanofibrils for efficient water reuse. J. Membr. Sci. 688, 122125.

Zhu, C.Y., Zhang, X., Xu, Z.K., 2020a. Polyamide-based membranes consisting of nanocomposite interlayers for high performance nanofiltration. J Appl Polym Sci 138 (9), 49440.

Zhu, X., Cheng, X., Luo, X., Liu, Y., Xu, D., Tang, X., Gan, Z., Yang, L., Li, G., Liang, H., 2020b. Ultrathin thin-film composite polyamide membranes constructed on hydrophilic poly(vinyl alcohol) decorated support toward enhanced nanofiltration performance. Environ. Sci. Technol. 54 (10), 6365–6374.